JOURNAL OF GEOPHYSICAL RESEARCH, VOL. 99, NO. B6, PAGES 12,175–12,190, JUNE 10, 1994

Climatic, eustatic, and tectonic controls on Quaternary deposits and landforms, Red Sea coast, Egypt

Raymond Arvidson,[1] Richard Becker,[1] Amy Shanabrook,[1] Wei Luo,[1] Neil Sturchio,[2] Mohamed Sultan,[1] Zakaria Lotfy,[3] Abdel Moneim Mahmood,[3] Zeinhom El Alfy[4]

Abstract. The degree to which local climatic variations, eustatic sea level fluctuations, and tectonic uplift have influenced the development of Quaternary marine and fluvial landforms and deposits along the Red Sea coast, Eastern Desert, Egypt was investigated using a combination of remote sensing and field data, age determinations of corals, and numerical simulations. False color composites generated from Landsat Thematic Mapper and SPOT image data, digital elevation models derived from stereophotogrammetric analysis of SPOT data, and field observations document that a ~10-km-wide swath inland from the coast is covered in many places with coalescing alluvial fans of Quaternary age. Wadis cutting through the fans exhibit several pairs of fluvial terraces, and wadi walls expose alluvium interbedded with coralline limestone deposits. Further, three distinct coral terraces are evident along the coastline. Climatic, eustatic, and tectonic uplift controls on the overall system were simulated using a cellular automata algorithm with the following characteristics: (1) uplift as a function of position and time, as defined by the elevations and ages of corals; (2) climatic variations driven by insolation changes associated with Milankovitch cycles; (3) sea level fluctuations based on U/Th ages of coral terraces and eustatic data; and (4) parameterized fluvial erosion and deposition. Results imply that the fans and coralline limestones were generated in a setting in which the tectonic uplift rate decreased over the Quaternary to negligible values at present. Coralline limestones formed during eustatic highstands when alluvium was trapped upstream and wadis filled with debris. During lowstands, wadis cut into sedimentary deposits; coupled with continuing uplift, fans were dissected, leaving remnant surfaces, and wadi-related terraces were generated by down cutting. Only landforms from the past three to four eustatic sea level cycles (i.e., ~300 to 400 kyr) are likely to have survived erosion and deposition associated with fluvial processes.

Introduction

Emerged Red Sea coastal deposits in the Eastern Desert of Egypt extend from the modern coral reefs to approximately 10 km inland to the contact with exposures of Precambrian rocks that are part of the Nubian Shield [*Veeh and Giegengack*, 1970; *Issawi et al.*, 1971; *Butzer*, 1976; *Greene*, 1984; *Said*, 1990; *Luo*, 1992; S. El Akkads and A. Dardir, unpublished map, 1965] (Figure 1). The overall tectonic setting is one of uplift associated with Red Sea rifting processes [e.g., *Steckler*, 1985; *Buck*, 1986; *Garfunkel*, 1988]. A number of normal faults run parallel to the coastline, with down dropped blocks on the seaward sides of the faults [*Sabet et al.*, 1973a,b; 1976; *Greene*, 1984]. The coastal plain deposits consist of Miocene to Holocene limestones, evaporite deposits, and alluvium derived from Precambrian exposures [e.g., *Greene*, 1984]. Several discrete coral terraces are also evident along the coastline, and a modern coral reef exists in regions that do not receive a high flux of wadi sediment.

Coastal landforms and deposits between the towns of Quseir and Marsa Alam (Figure 1) were the focus of our work in the 1991-1992 and 1992-1993 field seasons. The features of interest were (1) alluvial fans with relict surfaces, (2) throughgoing fluvial channels (wadis) and associated terraces; and (3) uplifted coral terraces near the current shoreline. Both relict fan and terrace surfaces were found to be covered by desert pavements. Further, examination of wadi walls showed several areas where alluvium is interbedded with coralline limestones, at elevations up to ~120 m above the current sea level. The alluvium and coralline limestones are of Quaternary age, given that these units are superimposed on sedimentary deposits of Miocene to late Pliocene age.

In this paper we quantify the nature and origin of the Quaternary fluvial and marine deposits and landforms in the study area. We determine geologic relationships between the marine and alluvial deposits, provide age constraints from U/Th dating of corals, and consider the overall system based on a cellular automata approach to modeling climatic, eustatic sea level, and tectonic uplift controls on fluvial erosion and deposition. The geology of the landforms and deposits is described first. Coral ages are then discussed, along with other constraints on the evolution of the fluvial and marine deposits and landforms. Next, a cellular automata model is presented, and implications are discussed as to the extent to which climatic fluctuations, eustatic sea level variations, and

[1]McDonnell Center for the Space Sciences, Department of Earth and Planetary Sciences, Washington University, St. Louis, Missouri.
[2]Argonne National Laboratory, Argonne, Illinois
[3]Ain Shams University, Cairo, Egypt.
[4]Egyptian Geological Survey and Mining Authority, Cairo, Egypt.

Paper number 94JB00037.
0148-0227/94/94JB-00037$05.00

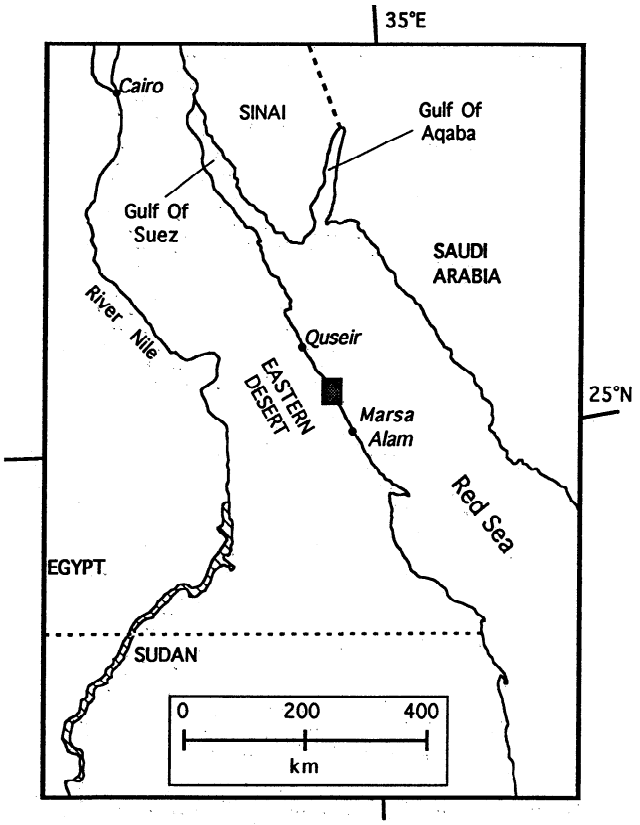

Figure 1. Location of study area between Quseir and Marsa Alam, Red Sea coast, Eastern Desert, Egypt. Also shown as a stippled box is the footprint of the merged Landsat TM and SPOT image color composite of Figure 3. Coastal deposits extend 10-15 km inland from the shoreline.

uplift have controlled the evolution of the deposits and landforms of interest.

Remote Sensing and Geologic Observations

The approach to understanding the geology of the coastal plain landforms is based on a combination of remote sensing data analysis, detailed field work in key areas, and synthesis of previous work. For lithologic unit discrimination, processed Landsat thematic mapper (TM) data were used to portray differences in major rock types. Figure 2 presents laboratory spectra of two minerals (calcite and gypsum) and a varnished cobble derived from a relict fan surface. The source of the cobble is the Precambrian Igla Formation, a dark metamorphosed graywacke [*Sabet et al.*, 1973a]. The gypsum and calcite data are for powders in order to maximize depths of absorption features. The locations of the TM passbands for the channels in the visible and reflected infrared are also shown. Gypsum and calcite have high radiance factors (i.e., reflectance) in the visible and show deep absorption features in the infrared. The calcite features are due to overtone and combination vibrations of carbonate anions, whereas the gypsum features are due to combinations and overtones from bound water molecules and from sulfate anions [*Hunt*, 1977]. Note that the gypsum sample has a particularly low band 7 value as compared to the calcite. On the other hand, the clast has a low, flat spectrum because of a coat of desert varnish 10-50 μm in thickness and because the Igla Formation is intrinsically dark [*Rivard et al.*, 1992]. In a TM color composite with band 1 assigned to blue colors, band 4 to green colors, and band 7 to red colors, regions with gypsum should appear bluish-green, areas with limestones should be whitish, and areas with desert pavements derived from Igla Formation debris should be a dark gray color.

Plate 1 is color composite with hue and saturation controlled by TM bands 1, 4, and 7, and intensity by a SPOT image acquired in panchromatic mode. The SPOT data have 10 m pixels as opposed to the 30 m TM pixels. The effect is to overlay the lower resolution TM color hue and saturation data over the SPOT intensity data. The Precambrian Igla Formation dominates outcrops in the Precambrian terrain. This unit shows as dark grays, browns, and reds. The large oval granitic intrusion called Umm Kadabora is also evident in the composite as a brownish unit with NNW-SSE ridges. The ridges are dikes composed of resistant pegmatites. The Miocene Gebel El Rusas Formation [*Greene*, 1984] forms the reddish brown outcrops adjacent to the Precambrian exposures. This formation is a mix of clastic deposits and coralline limestones. The color in the composite is controlled by the presence of ferric oxyhydroxides (e.g., limonite), which tend to have positive spectral reflectance slopes, thereby producing reddish brown colors in the 1, 4, 7 composite. The Pliocene Evaporite Formation,

Plate 1. False color composite of portion of study area generated using TM bands 1, 4, and 7 (0.45-2.35 μm) to provide hue and saturation and a SPOT panchromatic image to provide color intensity. In the panchromatic mode, the SPOT wavelength coverage extends from 0.50 to 0.90 μm. In effect, the composite has TM bands 1, 4, and 7 assigned to blue, green, and red colors, whereas the overall brightness is governed by the higher-resolution SPOT data (10 m pixels as opposed to 30 m pixels for TM). North is toward the top. Major wadis are labeled, and the coastal road is evident. Large white arrows aligned NW-SE denote the boundary between Precambrian outcrops of the Nubian Shield and coastal plain. Precambrian outcrops are dominated by the metasedimentary Igla Formation, a dark, dense graywacke, and by the granitic intrusion Umm Kadabora. The granite body is the oval feature located at coordinates H to L and 1 to 3. Coastal sedimentary rocks and sediments dip toward the Red Sea. The oldest unit evident is the Miocene Gebel El Rusas Formation, which corresponds to the reddish brown units adjacent to the Precambrian outcrops. The Pliocene Evaporite Formation appears as blue-green areas ~5 km inland (e.g., A to B; 1 to 2). The late Pliocene Gasus Formation (conglomerates, claystones, limestones) is exposed by faulting at location G to J, 4 to 6. The white areas adjacent to the coast are coral terraces. The blue and bluish-green areas near the coast are recent sabkha deposits. A number of dissected alluvial fans are also evident. In a few localities the fans have been displaced by faulting (e.g., D to E, 3 to 4). Darker areas on fans are relict surfaces that are topographically higher regions with dense pavements of dark clasts derived from underlying alluvium. The area analyzed in more detail with SPOT data is shown enclosed by a white box. Locations a, b, c, and d correspond to field photographs shown in Figures 3, 4, 5, and 8, respectively. TM scene 84/11/18/07/37/34 was acquired with solar elevation angle of 41°; SPOT 2 HRV scene 92/09/25 was acquired with a 61° solar elevation angle.

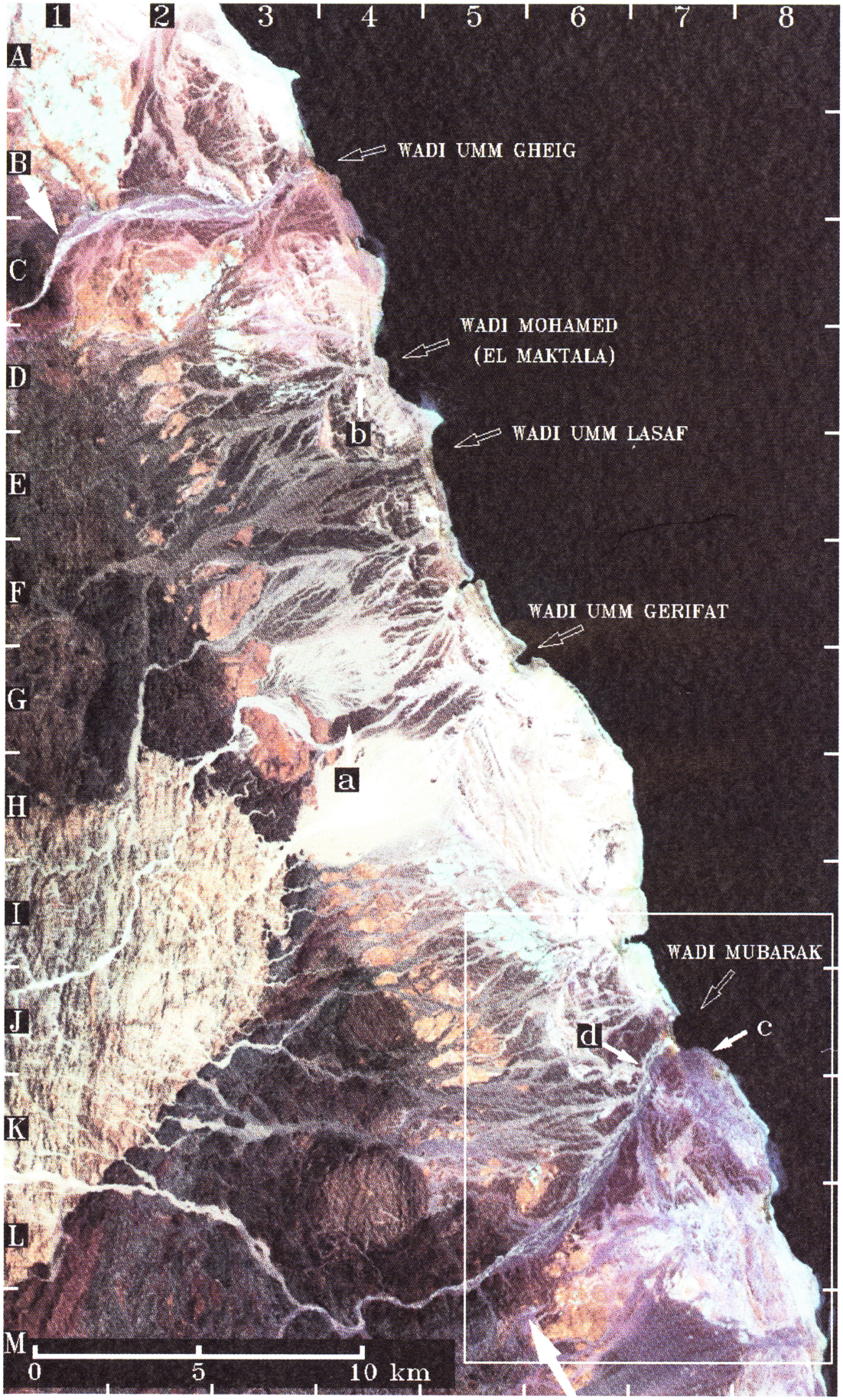
1
2
3
4
5
6
7
8
A
B
C
D
E
F
G
H
I
J
K
L
M
WADI UMM GHEIG
WADI MOHAMED
(EL MAKTALA)
WADI UMM LASAF
WADI UMM GERIFAT
WADI MUBARAK
a
b
c
d
0
5
10 km

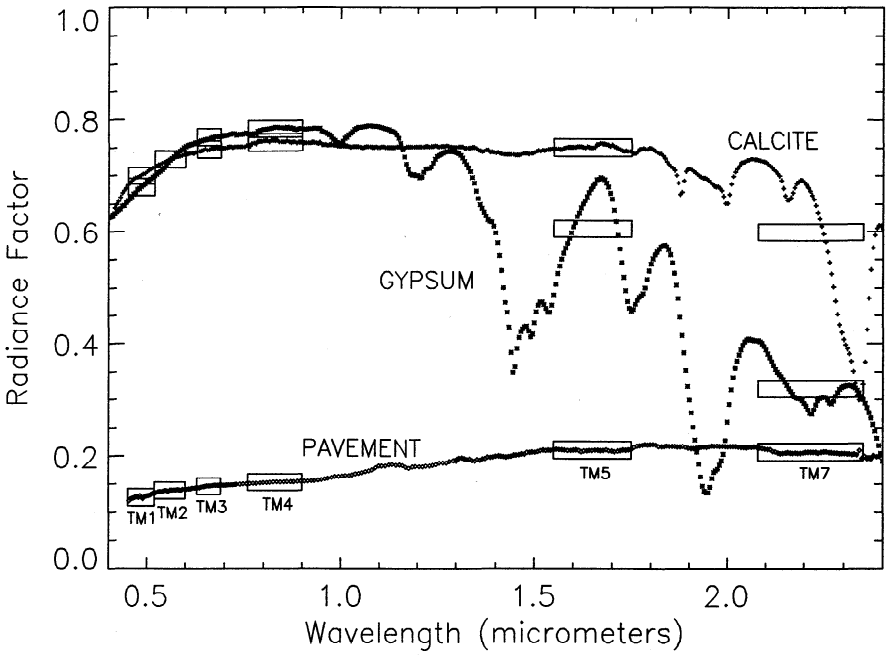

Figure 2. Reflectance spectra of a varnished metasedimentary clast from an alluvial fan, powdered calcite and powdered gypsum. Values are expressed as radiance factors, which are defined as the radiance from the sample divided by the radiance from a unit brightness Lambertian surface viewed at 0° incidence angle. The calcite and gypsum data were obtained using spectrometer facilities at Brown University [*Pieters*, 1983]. The clast data were obtained with a Daedalus Spectrafax AA440 Spectrometer [*Rivard et al.*, 1992]. Also shown are the radiance factors that would be obtained if the spectra were sampled by the relevant Landsat TM imaging system passbands.

which is dominated by gypsum [*Greene*, 1984], shows as blue-green outcrops, as predicted from reflectance spectra. Uplifted blocks of the late Pliocene Gasus Formation [*Greene*, 1984] are evident to the east of the Evaporite Formation. The Gasus formation consists of claystones, conglomerates, coralline limestones, and minor evaporite facies and, as a consequence, ranges in color from white to reddish brown. Field measurements show that the Miocene and Pliocene formations dip 10° to 30° toward the Red Sea. Alluvial deposits, including well-developed fans, drape over the Miocene and Pliocene units. In places, wadis have also cut through both the Miocene and Pliocene formations. The fans are best developed in areas where faulting has been minimal near the coastline. In several areas near the coast it also appears as if the fan deposits have been displaced by faulting. Finally, the whitish areas along the coast correspond to outcrops of coralline limestone associated with coral terraces, as predicted from the spectra in Figure 2, and the cyan to green areas near the coast delineate recent sabka deposits.

As noted, the alluvial fan deposits cover the Miocene Gebel El Rusas Formation and Pliocene Evaporite and Gasus Formations, thereby placing the alluvium deposits as Quaternary in age. The fans in the study area are typically dissected by a combination of throughgoing and local wadis. Field measurements indicate that the relict fan surfaces are elevated from several meters to up to ~30 to 40 m above active wadi floors. For material derived from the Igla Formation, dense desert pavements cover the relict surfaces and are underlain by up to ~1 m of aeolian accretion mantle (Figure 3). The highest relict surfaces are typically the darkest because they are covered with the densest desert pavements, i.e., the highest areal fraction of dark, varnished clasts derived from the Igla Formation. This pattern is interpreted as indicative of relative age, in that older relict surfaces would have more time than younger surfaces to develop mature desert pavements.

Field observations along wadi walls show interbedded alluvium and coralline limestones (Figure 4). At Wadi Umm Gheig, coralline limestone was found interbedded with alluvium within ~100 m of the edge of outcrops of the Igla Formation. In places the interbedding is also evident along the coastline (Figure 5). In areas where faulting close to the coast has precluded extensive growth of fans and alluvium, three overlapping coral terraces can be found, with heights of 6-8 m, 10-12 m, and 12-16 m. Also, a 1- to 2-m marine terrace can be found in some places just landward of the modern reef.

In addition to relict alluvial fan surfaces, the throughgoing wadis in the study area exhibit several fluvial terraces. Figure 6 is a portion of a SPOT image covering the distal part of Wadi Mubarak, and Figure 7 is an enlargement of the wadi where it enters the Red Sea. The distal end of the wadi is clearly an estuary (in Arabic a "Marsa", which translates as "safe harbor"). The narrow bright zone just off shore is the edge of the modern coral reef, and the bright deposits close to the shoreline are coral terrace outcrops. In fact, the coral outcrop shown in Figure 5 is located along the road ~200 m to the south of Wadi Mubarak. The dark areas in Figures 6 and 7 are dense desert pavements on relict alluvial fan surfaces and on fluvial terraces associated with Wadi Mubarak. Figure 8 is a ground view showing four distinct terraces on the southern side of Wadi Mubarak. Details of terrace heights for Wadi Mubarak and other wadis in the study area are given in Table 1.

To quantify the topographic relationships evident in the SPOT data of Wadi Mubarak and other field sites, a digital elevation model was generated from a pair of scenes by the TRIFID Corporation, St. Louis, Missouri. Data were obtained at 50-m intervals for selected areas of interest, after first using four control points and the coastline to update spacecraft position, velocity, and pointing information. Automatic point matching using a cross correla-

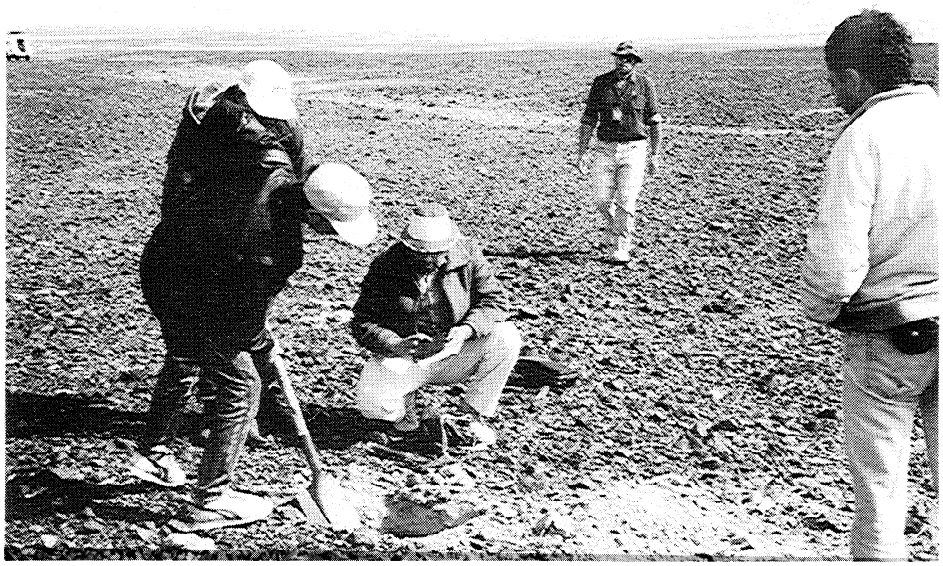

Figure 3. Desert pavement and underlying aeolian accretion mantle formed on a relict alluvial fan surface to the north of Wadi Umm Gerifat (location a in Plate 1). Pavement clasts are derived from the Igla Formation and are intrinsically dark. The dense, interconnecting pavement of clasts explains the low reflectance of the terraces formed on alluvium with these materials. Underlying the clasts is up to a meter thick deposit of wind-blown clay and silt-sized particles intermixed with alluvium. The relict surface is 8 m above the active wadi floor.

tion technique was used to determine parallax and to compute elevation. The resultant elevation model is thought to be good to within 15 m absolute elevation. Experiments in areas for which we have field measurements of heights demonstrate that the elevation model is good to within a few meters relative, i.e., in terms of local elevation differences. The elevation model shows that Wadi Mubarak has a gradient of 2%, rising to ~200 m above sea level for the area located in the lower left part of Figure 7. The elevation model also reinforces our observations that major wadis have as many as four terraces and that relict fan surfaces range in height from several meters to 30 to 40 m above current wadi floors.

Another constraint on the evolution of coastal deposits and landforms is the fact that alluvium is interbedded with coralline limestone. The outcrop shown in Figure 5 is particularly illustrative in that alluvium is at the bottom of the section and gives way to a fine-grained limestone. This unit in turn is replaced by a con-

Figure 4. Southern wall of Wadi Mohamed (El Maktala) showing interbedded alluvium and limestone (location b in Plate 1). Alluvium is found at the bottom of the section (lower right in the photograph). Coral reef deposits extend from the waist to above the head of geologist Zakaria Lotfy. An interpretive section is present in Figure 9.

Figure 5. Six to eight meter high marine terrace to the south of Wadi Mubarak (position c in Plate 1). The terrace consists of corals overlain by alluvium. Note the coral blocks weathered from the terrace face and mass wasting downhill. The top of the cliff is part of the extended surface of terrace 3 of Wadi Mubarak. Sample 19-3, Table 2, is from this coral outcrop.

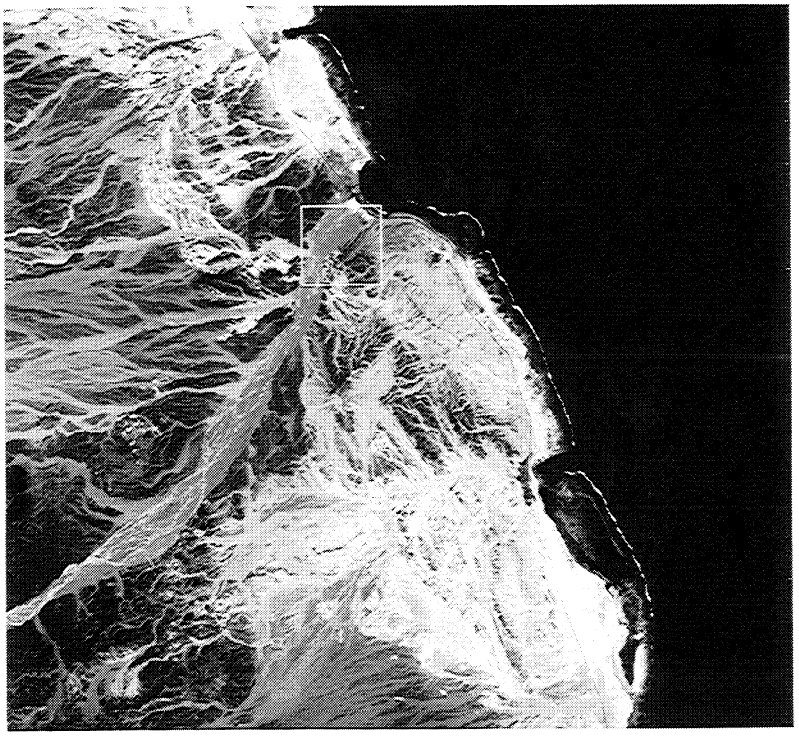

Figure 6. Distal portion of Wadi Mubarak (large channel running from lower left to upper right) as obtained by the SPOT image system in panchromatic mode. Box corresponds to area shown in enlarged form in Figure 7. The narrow, bright zone offshore is a surf zone delineating the edge of the modern Red Sea coral reef. The coastal road can be seen. The bright areas between the coastal road and the shoreline correspond to coral terrace outcrops. Dark areas on the image are covered with desert pavements and are associated with relict alluvial fans and terraces associated with Wadi Mubarak.

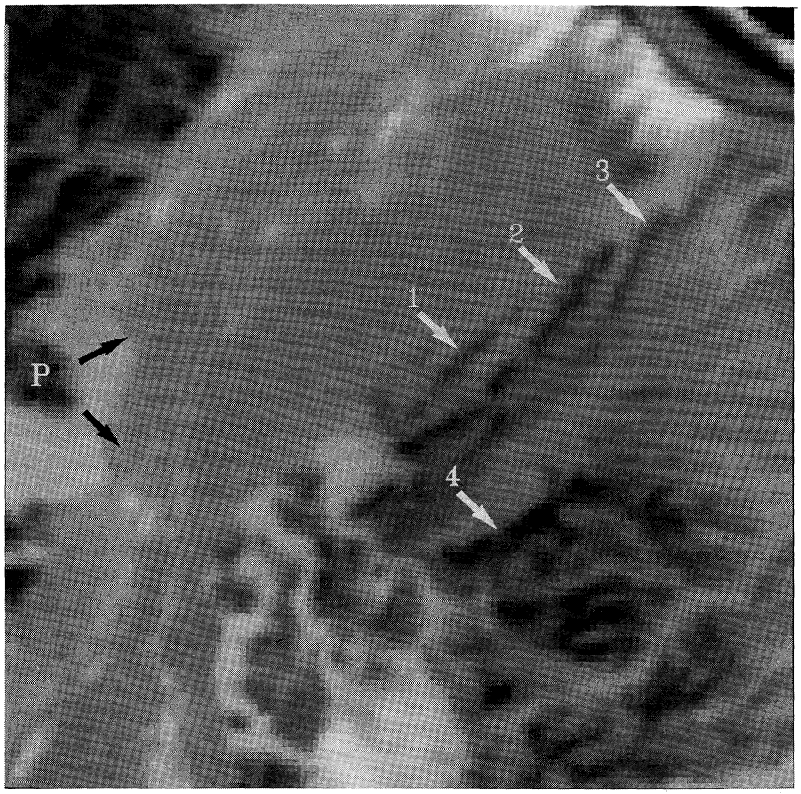

Figure 7. Enlargement of boxed area in Figure 6. Arrows point to four terraces on the southern side of Wadi Mubarak. These areas are presented from a ground perspective in Figure 8. The letter "P" marks the site at which the ground photograph was acquired, and solid arrows outline the approximate field of view of Figure 8. Terraces on the southern side of Wadi Mubarak are also delineated by arrows and numbers.

Figure 8. View of the four terraces associated with the southern wall of Wadi Mubarak. Terraces are delineated with arrows and numbers. Heights are presented in Table 1. The Red Sea can be seen at the upper left. Note the desert pavement development at the site from which the image was acquired: terrace 3 on the northern side of Wadi Mubarak (location d in Plate 1). Terrace 4 is highly dissected, consistent with its high elevation and inferred antiquity as compared to terraces 1 to 3.

Table 1. Fluvial Terraces Associated With Selected Wadis

Wadi	Location	Terrace Heights Above Wadi Floor, m
Umm Khariga	25°3′48″N; 34°50′0″E	1-2; 6-7; 12-14
Seifan	25°6′5″N; 34°51′38″E	2-3; 4; 6; 10
Mubarak	25°30′32″N; 34°38′48″E	1-2; 8-14; 20-22
Umm Gheig	25°43′16″N; 34°32′24″E	1-2; 5-8; 13; 20-30

Data were acquired using a tape measure and inclinometer. Observations were made where terraces are well-developed, which is typically less than several kilometers from the coast.

glomerate composed of rounded fragments of disrupted coral reef. Corals in growth position are next, and the top of the section is occupied by alluvium (Figure 9). This section can be interpreted using concepts from dynamic stratigraphy [e.g., *Matthews and Frohlich*, 1987] as follows: the transition from the lower alluvium to the fine-grained limestone is due to submergence that trapped alluvium upstream and led to deposition of carbonates. The fine-grained limestone formed in a back reef or estuarine environment. The coral conglomerate is interpreted as a storm deposit. Further submergence led to formation of a coral reef. Finally, the upper unit (alluvium) is a consequence of progradation of alluvium over the corals, since the whole region has been subjected to uplift associated with rifting processes. Continued uplift supplied energy to the fluvial system (in terms of grade) and thus the fluvial deposits eventually prograded to the sea.

In summary, what is observed in the study area is a set of coalescing alluvial fans of Quaternary age beginning at the interface between the rugged Precambrian exposures and the coastal deposits. The fans are dissected, with remnant surfaces as high as 30-40 m above active wadi floors. Further, major wadis typically have four fluvial terraces. Interbedding between coralline limestones and alluvium is found from the coast to within ~100 m of the contact with Precambrian units. Given that corals only grow in shallow water, determination of coral ages would provide a first-order constraint on the uplift history of the study area. Age data for coral samples and inferences are discussed in detail in the next section.

Uranium-Thorium Disequilibrium Dating of Marine Terraces

A major part of our 1992-1993 field season was dedicated to collecting in-place coral samples for U/Th disequilibrium dating. A key requirement was to find samples that have not undergone the aragonite to calcite transition, i.e., samples that have remained in a closed system since the corals formed. Four coral terraces, adjacent to the coastline at heights of 1-2, 6-8, 10-12, and 12-16 m above sea level were examined at a dozen localities within the study area. Collection sites ranged from Marsa Alam on the southern boundary of the study area to north of Wadi Umm Gheig. The majority of the samples were collected from the upper portion of each terrace, and float or nongrowth position corals were carefully avoided [e.g., *Chen et al.*, 1991]. Massive, coherent corals were broken into sections, and samples were taken from the cores of the structures rather than the perimeters. The more massive coral varieties, such as the brain corals, were sampled preferentially over branching or dendritic corals [e.g., *Bloom et al.*, 1974]. Finally, although color and texture were not rigid standards for selection, the whiter and more resistant corals were selected over discolored or fragile samples. After collection, samples were rinsed in deionized water, etched in HCl, and stained with Feigel's solution in the field [*Friedman*, 1959; *Schneiderman and Sandberg*, 1971]. Only samples that indicated high aragonite content were collected and used in subsequent analyses.

For U/Th dating, interior portions of aragonitic samples were prepared by cutting and/or chiseling, and all saw or chisel marks and exterior (weathered) surfaces were removed by grinding. Deionized water was used as a lubricant for all cutting and grinding operations. Sample blocks (~10 to 100 g) were thrice cleaned ultrasonically in deionized water, dried at room temperature, and gently crushed (to <1cm) prior to dissolution. Splits of the crushed samples were finely ground for X ray diffraction studies. Relative amounts of aragonite and calcite were estimated from the (110) aragonite peak area in relation to the (104) calcite peak area, as compared to mixtures prepared from known amounts of aragonite and calcite.

Measurements of Th and U isotope activities in coral samples were performed at Argonne National Laboratory by α spectrometry using procedures adapted from those described previously [*Sturchio and Binz*, 1988]. Reagent grade acids and ultrapure

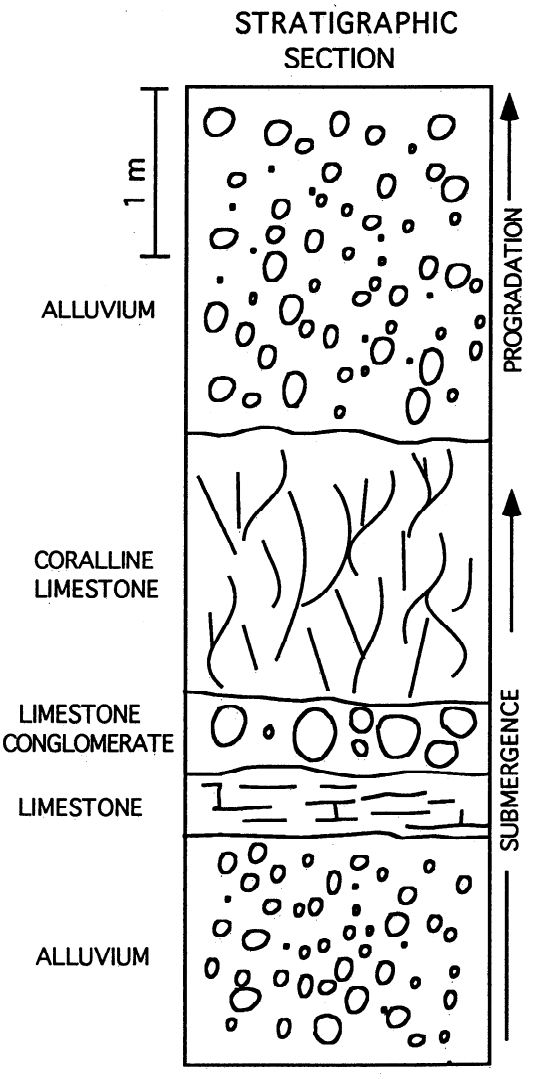

Figure 9. Stratigraphic column derived from southern wall of Wadi Mohamed (El Maktala).

Table 2. Summary of U/Th Disequilibrium Ages of Coral Samples Collected From Marine Terraces

Sample	Coral	Height Above Sea Level, m	U, ppm	$(^{234}U/^{238}U)$	$(^{230}Th/^{234}U)$	Age, kyr	$(^{234}U/^{238}U)_o$
7-4	Meandrina	6 to 8	2.73±0.05	1.12±0.03	0.650±0.020	111±6	1.16±0.03
7-8	Septastrea	6 to 8	2.96±0.04	1.11±0.02	0.685±0.018	122±6	1.16±0.03
10-3	Meandrina	3	2.36±0.03	1.08±0.02	0.713±0.019	133±7	1.12±0.03
11-5	Meandrina	8 to 10	2.83±0.04	1.14±0.02	0.681±0.018	120±6	1.19±0.03
12-1	Septastrea	3	2.39±0.06	1.15±0.03	0.620±0.022	102±6	1.20±0.04
13-1	Favia	6	2.42±0.04	1.13±0.02	0.658±0.019	113±6	1.18±0.03
17-2	Undeterm.	1 to 2	3.08±0.09	1.11±0.03	0.650±0.025	112±7	1.15±0.04
19-3	Undeterm.	6 to 8	2.45±0.04	1.14±0.04	0.928±0.035	$248^{+38}/_{-29}$	1.28±0.07
11-8 A*	Undeterm.	10 to 12	2.34±0.04	1.04±0.02	1.123±0.033	——	——
11-8 B*	Undeterm.	10 to 12	3.17±0.06	1.03± 0.03	1.015±0.030	≥370	——

Samples 7 to 17 were collected within 15 km to the north of Marsa Alam. Sample 19-3 is from the outcrop to the south of Wadi Mubarak shown in Figure 5; analyzed samples have <0.01 ppm Th and values of $(^{230}Th/^{232}Th) >$ 1000. Decay constants used in age calculations: $\lambda\ ^{230}Th$, $9.195\times10^{-6}y^{-1}$; $\lambda\ ^{234}U$, $2.835\times10^{-6}y^{-1}$; $\lambda\ ^{238}U$, $1.551\times10^{-10}y^{-1}$. Uncertainties are ±1σ, based on counting statistics.

*A, whole sieved sample (75 to 150 mesh); B, fraction of sieved sample having specific gravity > 2.9.

deionized water were used for all chemical procedures. To dissolve the carbonate fraction of the coral samples, a weighed portion (~5 g) of each sample was placed in a beaker and covered with deionized water, and dilute nitric acid was added slowly in increments sufficient to obtain gentle decarbonation. Acid molarity in the beaker ranged from 0.1 to 0.3 *M* during this procedure. When sample decarbonation was complete, undissolved residue was removed by centrifugation. Precisely measured amounts of a $^{229}Th/^{236}U$ spike solution calibrated against NBS-610 were added to supernate solutions. The solutions were equilibrated on a warm hot plate overnight, then slowly evaporated to dryness. The sample was then redissolved, and Th and U were coprecipitated with $Fe(OH)_3$ and purified using anion chromatography. Purified Th and U were electrodeposited onto stainless steel planchets, and al-

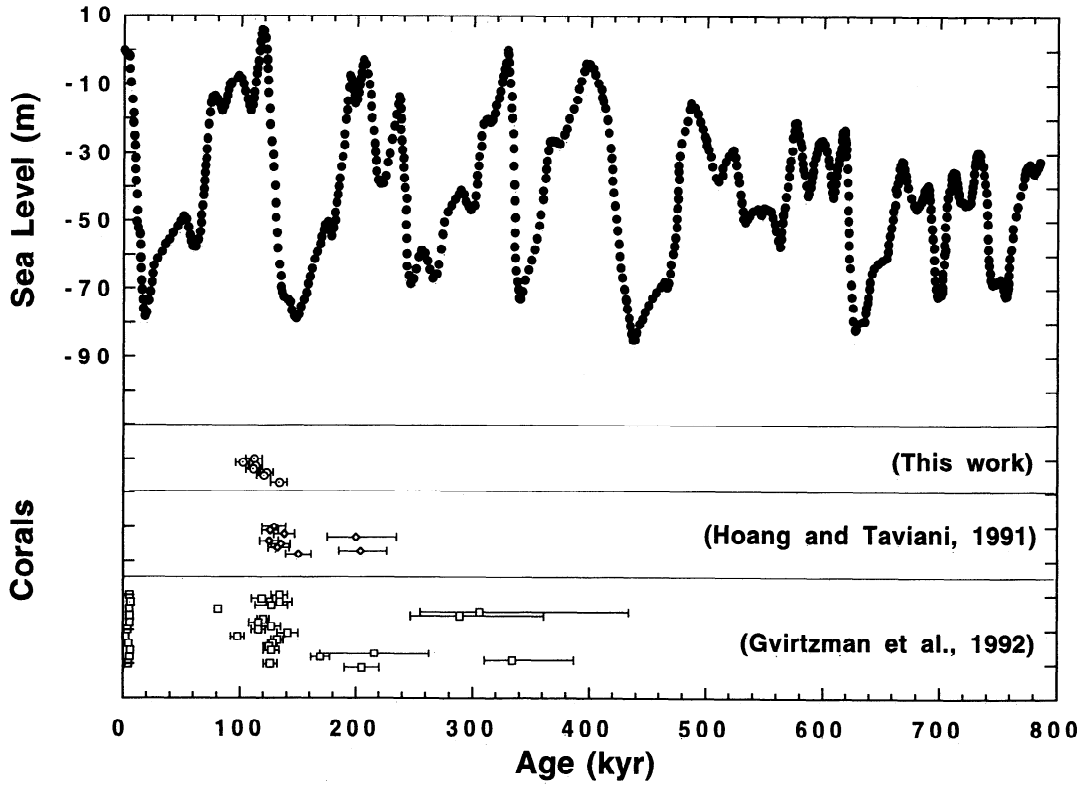

Figure 10. Eustatic sea level fluctuations for the past 800 kyr, from *Imbrie and Imbrie* [1980]. Also shown are U/Th ages (and 1σ errors) for corals obtained as part of this study and as reported in previous work. Note the correspondence between coral ages and the 120 kyr eustatic sea level high stand. Corals from the study area (and Red Sea coast in general) that are older than 120 kyr have large errors, although a correlation with older highstands can be discerned.

pha spectra were acquired using low-background Si surface barrier detectors. Total procedural blanks were <0.4% of sample U and Th. Results are reported in Table 2. Based on X ray diffraction analyses, all samples except sample 11-8 had at most only a few percent calcite. Sample 11-8 had ~10% calcite. Further processing was done on this sample by crushing a portion and using a heavy liquid to separate the aragonitic portion. Both the bulk and aragonitic portions are reported in Table 2.

Data for the first seven samples in Table 2 show a strong cluster of ages with a mean value of 116 kyr. The $^{234}U/^{238}U$ initial values are equal to that of modern seawater (1.14) to within 2σ error. These samples were all collected from either the first or second marine terrace exposed landward of the modern shoreline. The ages imply that the corals associated with the first two terraces formed during the last major highstand (~120 kyr), when sea level was approximately 6 m higher than present [e.g., *Imbrie and Imbrie*, 1980]. Thus, the 1- to 2-m marine terrace found in the study area is probably a wave-cut bench, perhaps generated during the well-known climatic optimum (~6 kyr) when sea level was 1-2 m higher than present. We find no evidence for the 75- or 90-kyr terraces at 8 m reported by *Veeh and Giegengack* [1970]. Data for the last three samples reported in Table 2 are of questionable quality. The $^{234}U/^{238}U$ initial value for 19-3 is 1.28, implying that the sample has not remained a closed system. Samples 11-8A and 11-8B are too old to be dated with U-Th disequilibrium techniques.

Figure 10 is a plot of eustatic sea level fluctuations over the past 800 kyr, as inferred by *Imbrie and Imbrie* [1980] from oxygen isotopic data for marine microfossils. Also shown in Figure 10 are our U/Th ages, ages for corals to the north of our study area [*Hoang and Taviani*, 1991], and results from a study of uplifted coral terraces exposed along the southeast Sinai coastline [*Gvirtzman et al.*, 1992]. The correlation with the 120-kyr highstand is well illustrated by the plot. There does appear to be a cluster associated with the 200-kyr highstand and perhaps with the 320-kyr highstand, although the large errors associated with old ages makes the correlations difficult to confirm in a statistical sense. However, given the evidence just presented, and the global correlation of coral terrace ages with highstands [e.g., *Bloom et al.*, 1974], it is reasonable to conclude that the uplifted coralline limestones of Quaternary age along the Red Sea coast formed during previous highstands.

Constraints on Generation of Quaternary Deposits and Landforms

A primary external variable that needs to be considered in modeling the Quaternary deposits and landforms in the study area is the tectonic uplift history. Uplift relative to the geoid needs to be specified as a function of position and time. The 6- to 8-m coral terrace, dated at 120 kyr, demonstrates that the uplift rate has been negligible over that time period, since sea level was 6-8 m higher during this period (e.g., Figure 10). As noted, two other coral terraces are found just inland of the 6- to 8-m terrace, at heights of 10-12 m and 12-16 m, respectively. These two terraces are interpreted to have formed during the 200- and 320-kyr highstands (e.g., Figure 11). Given that these highstands were of the magnitude of the current sea level value, the heights of these terraces thus directly indicate the amount of uplift relative to the geoid.

Additional information on uplift history is given by *Abdou* [1991], who worked in Wadi Ambagi to the west of Quseir. He mapped three coral terraces (6-8; 10-12; 14-16 m) on the coastline, along with four deposits of coralline limestone farther inland that are interbedded with alluvium. He interpreted the four deposits as older coral reefs that have been covered by alluvium and uplifted to their current positions. It is reasonable to assume that the four deposits correspond to older highstands as delineated in the data in Figure 10. With this assumption, a plot of height above current sea level verses age can be generated from our data and his

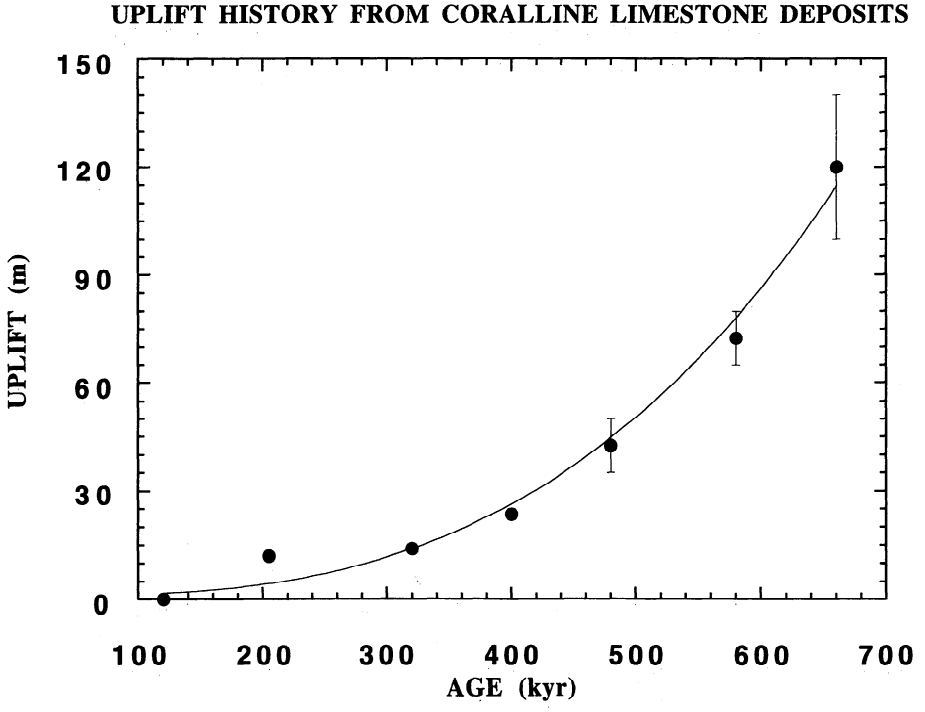

Figure 11. Uplift as a function of time for the study area using the correlations between coral terraces and coralline limestone outcrop heights and timing of highstands. An exponential function has been fit to the data. Error bars represent range of heights found for coralline limestone outcrops as reported by *Abdou* [1991].

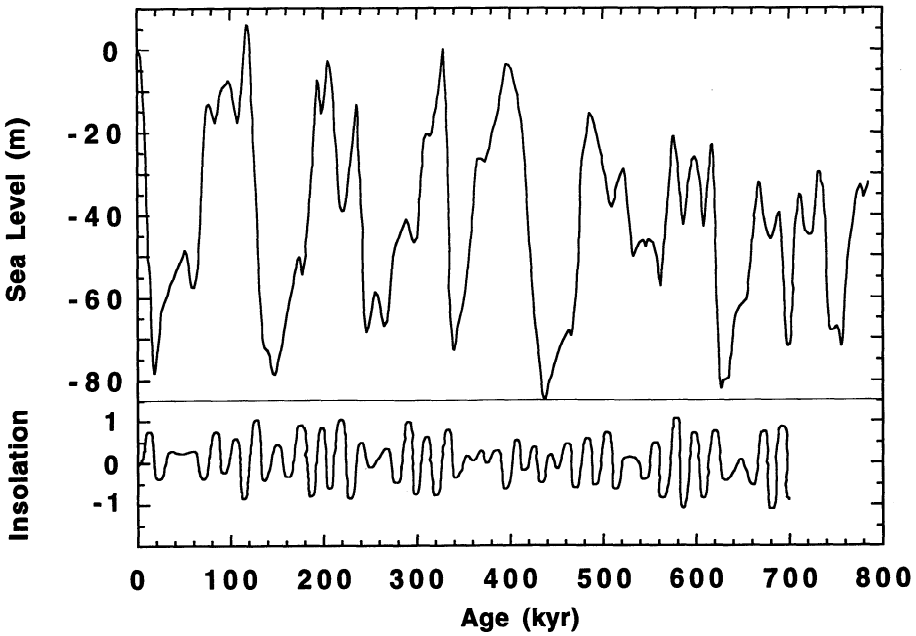

Figure 12. Eustatic sea level and Milankovitch cycle-related northern summer insolation variations. Adapted from *Imbrie and Imbrie* [1980] and *Matthews* [1974], respectively. Insolation curves are normalized to a range of 1.

data and an uplift rate as a function of time obtained (Figure 11). Results indicate that the uplift rate has declined exponentially over the Quaternary Period.

With regard to eustatic sea level effects, the data shown in Figure 10 were used to control the absolute height of sea level as a function of time. This is a reasonable approach, given that the Red Sea during the Quaternary Period remained connected to the Indian Ocean, even during glacial maxima and corresponding lowstands [*Behairy and Yusuf*, 1984; *Thunell et al.*, 1988]. As to variations in rainfall in the Eastern Desert, evidence suggests that the annual rainfall amount has been controlled by the intensity of the summer monsoons in the Indian Ocean. Wet periods in northeastern Africa correlate with periods of high northern summer insolation as inferred from Milankovitch cycles of obliquity, precession, and eccentricity [*Clemens et al.*, 1991]. For quantitative constraints we scaled the current rainfall of about 1 cm/yr to higher values during periods of increased insolation and to lower values during periods in which the insolation was lower. The peak value used was 20 cm/yr, a number obtained from examining annual rainfall records at the southern margin of the Sahara [*Thompson*, 1965]. Since the effect of increased monsoonal activity is to move the Sahel wetting front northward, this is a reasonable approach. A similar trade of time for space was used by *Koltermann and Gorelick* [1992] to constrain variations in rainfall over the Quaternary for modeling sediment accumulation in northern California. The combined eustatic and climatic controls are shown in Figure 12.

Numerical Simulations

The next step was to place the tectonic, eustatic, and climatic constraints in a context in which surface processes are modeled to first order. Based on the work on cellular automata techniques in geomorphology done by *Chase* [1992], our model is summarized

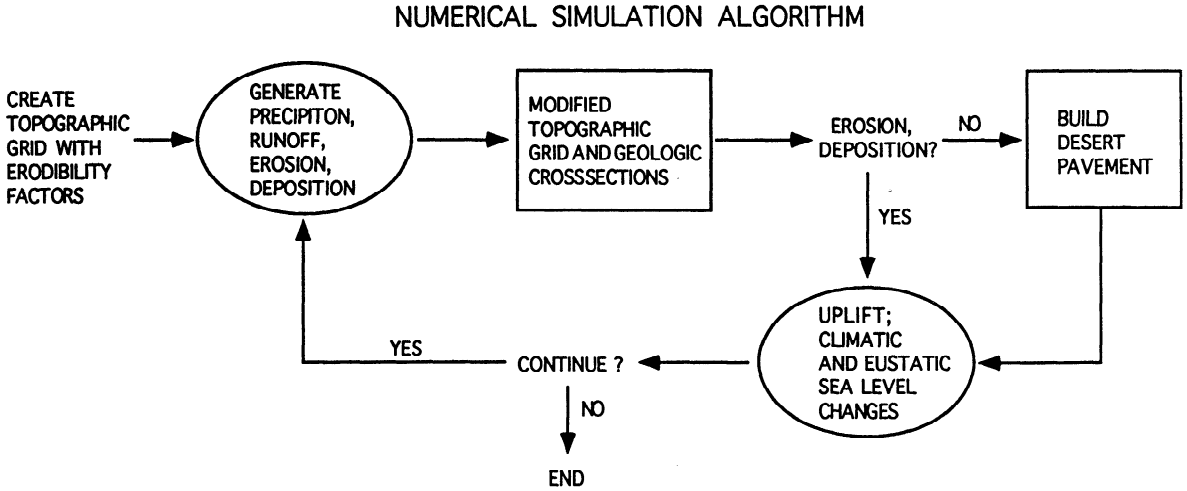

Figure 13. Flow diagram illustrating cellular automata approach to simulation of erosion, deposition, and desert pavement formation.

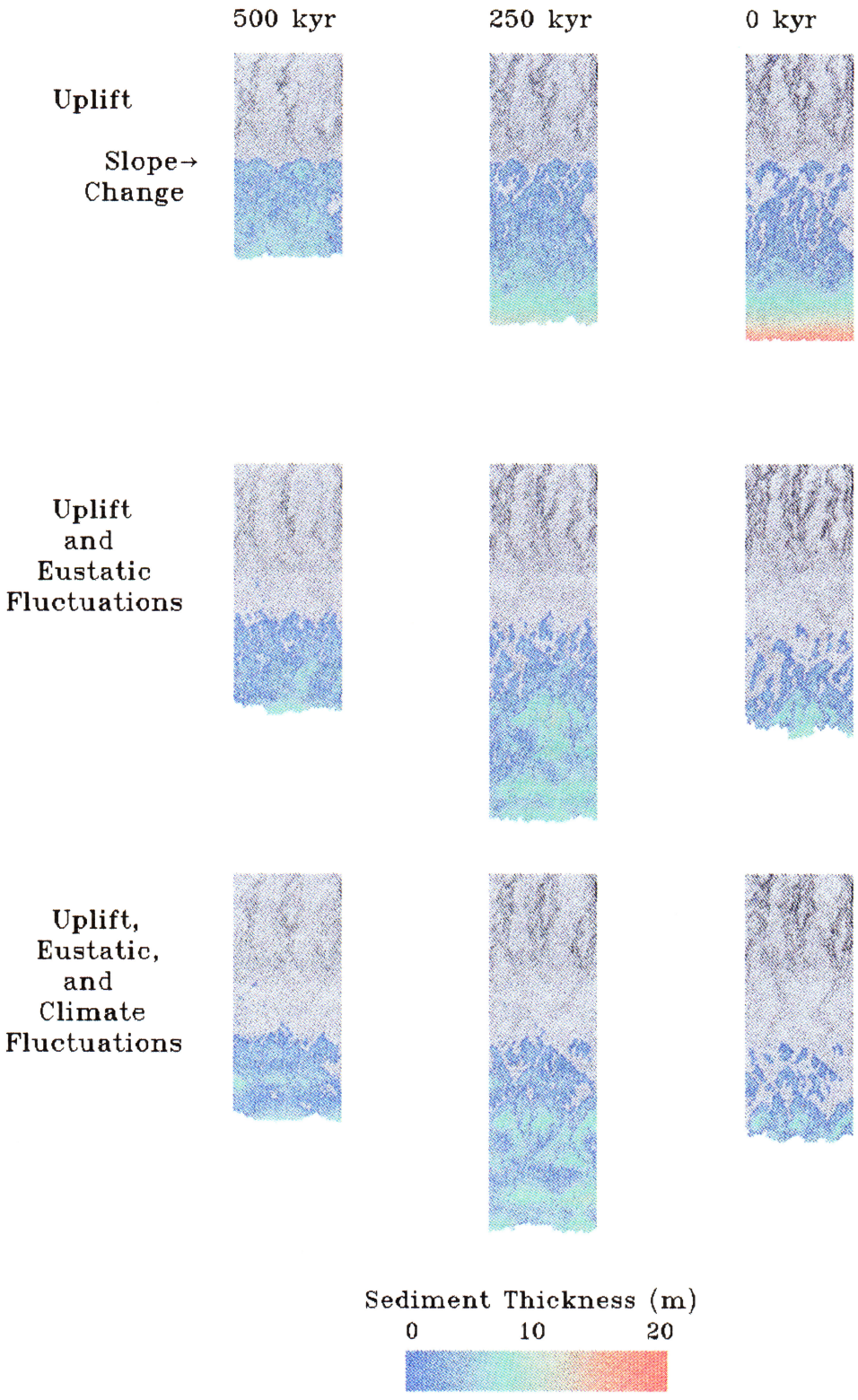

Plate 2. Colored-coded alluvium thicknesses (i.e., isopach contours) superimposed on bedrock shaded relief views. The width of each map is approximately 10 km which is resolved into 50 elements (i.e., cells) in the simulations. Bedrock shown in shaded relief form to emphasize channeling. The top series correspond to a run with uplift only. The middle includes uplift and eustatic sea level fluctuations. The bottom includes uplift, eustatic, and climatic fluctuations. Break in slope representing the Precambrian boundary with the coastal plain is shown. In each case, initial sea level was set at that location. The bottom of each map ends at the sea level relevant for the time and simulation shown. Seaward migration of sediment is evident in each case, including deposition over and then uncovering of bedrock close to the border with the Precambrian.

in the flow diagram shown in Figure 13. An extended grid is developed in which each element is initially assigned an elevation and erodibility. A precipiton (i.e., a parameterized rainfall event) of some intensity is then allowed to fall randomly on some cell on the grid, and the depth of erosion is scaled as the product of the sine of the slope angle (i.e., proportioned to shear force component) and a parameterized erodibility. The slope angle is based on the maximum difference of the topography of the current cell relative to the values for surrounding cells. Carrying capacity is defined as the product of precipiton intensity and the sine of the slope angle and is recomputed for every cell. Material is carried by surface flow to lowest adjacent cells. At any given cell location, if the new carrying capacity is exceeded, deposition occurs. Mass movements are modeled using Fickian diffusion as described by *Chase* [1992]. If no erosion or deposition occurs, a parameterized desert pavement is allowed to develop, so that the simulation tracks how long the surface has been inactive. Delivery of fluvial sediment into the sea is modeled by dropping the carrying capacity to a small value (0.20 of fluvial value), i.e., depositing the material.

After one precipiton cycle, the overall grid is subjected to uplift that varies with position and time within the model run. Sea level is moved up or down by some amount, depending on where the simulation is placed in the highstand-lowstand cycles. The number of precipitons per year is controlled by the northern summer insolation value to cover the 20 to 1 range in estimated annual rainfall amounts. Finally, the locations, thicknesses, and ages of fluvial deposits are tracked. Because of the small distances, and short time scale (1 m.y.) involved, isostatic readjustments due to erosion and deposition are ignored.

The cellular automata model is parameterized, with scaled values of precipiton intensity and erodibility. The intent is not to simulate all features of the deposits or landforms. Rather, the purpose is to run simulations that involve combinations of uplift, eustatic sea level and climatic variations to gain insight into the importance of each variable in generating and modifying the deposits and features. For simplicity, the precipiton intensity is set to unity. Thus the free parameters are the initial topography, the precipiton frequency, and the erodibility. We chose to simulate initial topography as a pair of planar surfaces, i.e., beginning with tilted peneplains. Surface slope was set at 1.5% grade for the coastal plain and 3.0% grade for the planar area representing the Precambrian zone. The uplift history is defined as in Figure 11 for the coastal zone and as 1.25 times that function for the Precambrian terrain. The intent was to simulate more rapid uplift of the Precambrian terrain relative to the coastal zone. A number of runs were conducted over 1- m.y. time periods with time-invariant values of precipiton frequency and erodibility values. Results for a run with precipiton frequency of 1 per year and a sediment erodibility 10 times that of bedrock are shown in Plate 2 in map form with isopach values and in Figure 14 as plots of sediment thickness versus horizontal distance. The sediment mass produced by erosion is typical of the amount of material produced from bedrock over ~1-m.y. timescale [*Garrels and Mackenzie*, 1971]. Further, runs conducted with initial surfaces that have been "conditioned" by erosion and deposition show no significant differences in the gross amount or pattern of sediment accumulation relative to beginning at 1 m.y. with tilted peneplains. Thus the conditions used in the run described in this paragraph were used as a baseline to explore effects of eustatic sea level and climatic fluctuations.

Runs were made for the same conditions as given in the above paragraph, with the additional constraint that sea level was allowed to vary based on the eustatic data given in Figure 10. Results are shown in Plate 2 and Figure 15. Finally, runs were made with both eustatic and climatic variations and exemplary results

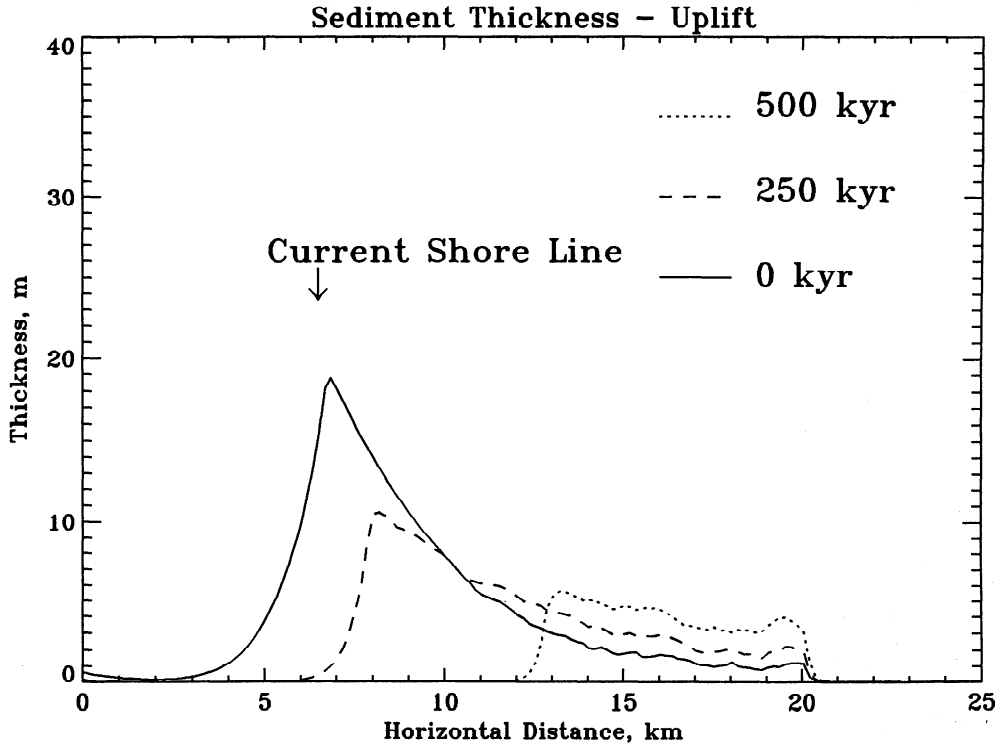

Figure 14. Plot of sediment thickness as a function of horizontal distance for three time intervals for the simulation of tectonic uplift and constant sea level and climate. Note the migration of sediment toward the sea as uplift continues from 500 to 0 kyr.

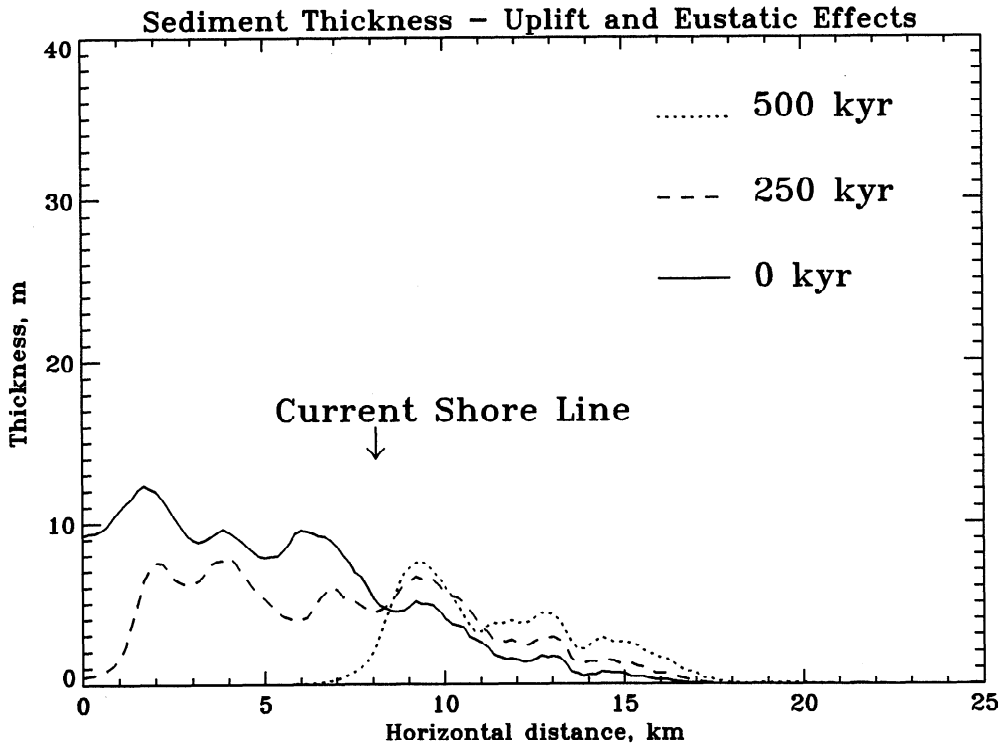

Figure 15. Plot of sediment thickness as a function of time for a simulation with uplift and eustatic sea level fluctuations. The climatic variable was kept constant. Note that the locus of sedimentation is shifted seaward relative to the simulation with uplift only. The shift is a consequence of lower base levels during lowstands. The peaks are associated with shallow marine clastic deposits produced during lowstands.

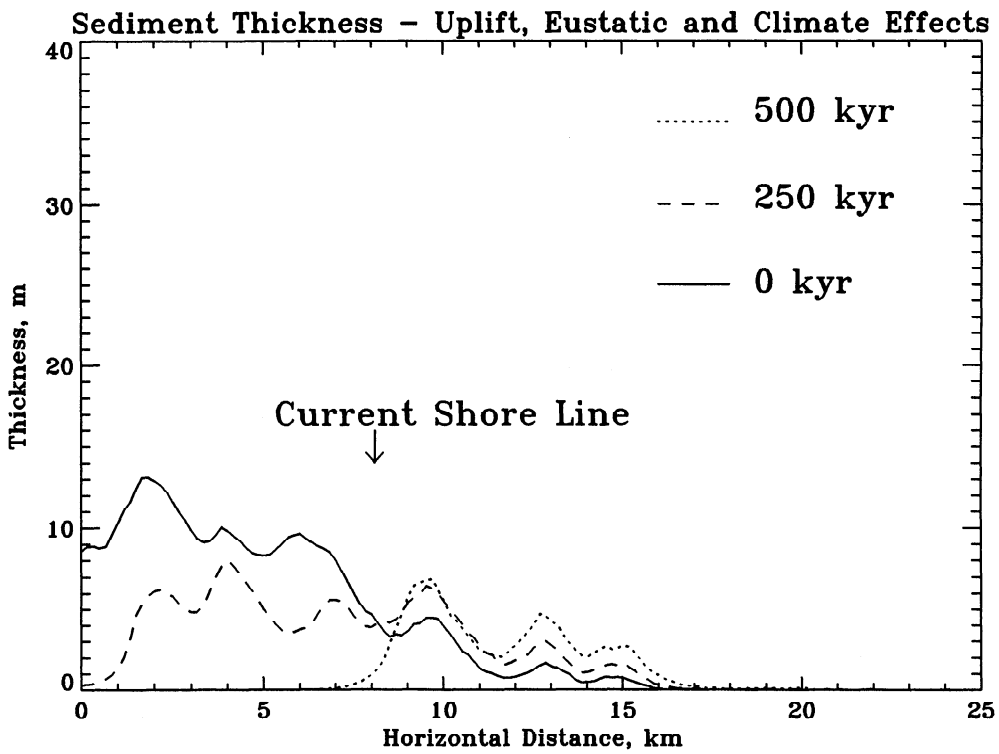

Figure 16. Plot of sediment thickness as a function of time for a simulation with uplift, eustatic sea level, and climatic fluctuations. Sediment is displaced seaward relative to the runs shown in Figures 14 and 15 because of the effect of wet periods during lowstands. The particularly erosive periods also cause removal of much of the evidence for previous sea level positions.

are given in Plate 2 and Figure 16. As noted, the purpose of the simulations is to provide insight into the relative importance of sea level and rainfall fluctuations in a coastal setting subjected to uplift.

The effect of eustatic sea level fluctuations with constant rainfall is to induce the system to seek different fluvial baselines at different times. The net result of the series of lowstands is a seaward displacement of sediment mass as compared to the runs that have uplift without eustatic sea level variations. Further, because of continued uplift, these profiles migrate seaward with time, producing sediment thickness plots with relict profiles that show as peaks several meters in thickness. Older peaks are smoothed by subsequent fluvial erosion and deposition. Tracking extent of desert pavement with the model shows that ~70% of the alluvial surfaces have been modified by erosion or deposition within the past 300 kyr.

The addition of rainfall fluctuations significantly modifies the surface and deposits. Examination of Figure 12 shows that the climatic fluctuations occur more frequently than eustatic sea level changes. Examination of simulation results over time intervals corresponding to dry-wet-dry periods demonstrates that a great deal of sediment is moved seaward when a wet period occurs during a lowstand, i.e., when the system adjusts to a lower base level during a period with numerous rainfall events. The effect is to move the sediment mass seaward of the case with only uplift and eustatic fluctuations. Also, since the rainfall events occur over small distances relative to effects of sea level fluctuations, another consequence is the enhanced destruction of the sediment peaks produced by eustatic effects. Pavement simulations show that ~90% of the surface has been modified over the past several hundred thousand years. Combined with the sediment distribution patterns, it is highly unlikely that surface features produced prior to 300-400 kyr. ago would be preserved.

Finally, although the model is not detailed enough to be able to generate fluvial terraces, their genesis and relationships to eustatic sea level are clear. During highstands, corals form as alluvium is trapped upstream. Wadis tend to fill. During lowstands, wadis cut into the alluvium and generate terraces. Thus the terraces have a direct relationship with coralline limestone deposits. For the case of Wadi Mubarak, the first terrace is interpreted to be associated with the 6-kyr climatic optimum highstand, the second terrace with the 120-kyr highstand, and the third terrace with the 200-kyr highstand. In fact, alluvium beneath the third terrace covers the deposit of coralline limestone shown in Figure 6, for which an age of ~248 ka is reported (Table 2), i.e., an age consistent with formation in association with the 200-kyr highstand and subsequent lowstand events. Consistent with our simulations and observations, the fourth and older terraces are highly dissected and relations with coralline deposits on the basis of landforms have been masked or removed by erosion and deposition.

Conclusions

Remote sensing, field, and laboratory data, together with numerical simulations, constrain the extent to which local climatic fluctuations, eustatic sea level variations, and tectonic uplift have controlled the development of the coalescing alluvial fans, fluvial terraces, and uplifted coralline limestones along the Red Sea coast, Eastern Desert, Egypt. Uplift decreased rapidly during the Quaternary period to negligible values at present. Coralline limestones formed during sea level highstands when sediment was trapped upstream. During lowstands, wadis cut into sedimentary deposits, and generated fluvial terraces. Slow uplift raised these deposits and dense desert pavements formed on the relict alluvium surfaces derived from resistant metasedimentary rocks.

Acknowledgments. This work was supported by the NASA Geology Program grant NAGW-1358 to Washington University. Access to the field and help with logistics was kindly provided as part of joint agreements for research between Washington University and the Egyptian Geological Survey and Mining Authority and Washington and Ain Shams Universities. We also thank Marshall Faintisch and Dennis Holdman, TRIFID Corporation, St. Louis, Missouri, for their production of digital elevation models from SPOT image stereo image data. Facilities for U series measurements at Argonne National Laboratory were supported by the Geosciences Research Program, Office of Basic Energy Sciences, U.S. Department of Energy, under contract W-31-109-Eng-38. Michael Ellis, Arthur Bloom, and Michael Jackson provided thoughtful reviews of an earlier version of this paper. Support for reproduction of color plates has been provided by NASA grant NAGW3338 to Michael A. Ellis.

References

Abdou, N.Y., Some geomorphic features of the coastal plain of the Red Sea, south of Gulf of Suez, Egypt, Ph.D. thesis, 464 pp., Ain Shams Univ., Cairo, Egypt, 1991.

Behairy, A.K.A., and N. Yusuf, Distribution of some planktonic foraminifera species in deep-sea cores from the Red Sea and their relation to eustatic sea level changes, *Palaeogeo. Paleoclimatol. Paleoecol., 46*, 291-301, 1984.

Bloom, A.L., W.S. Broecker, J.M.A. Chappell, R.K. Matthews, and K.J. Mesolella, Quaternary sea level fluctuations on a tectonic coast: New $^{230}Th/^{234}U$ dates from the Huon Peninsula, New Guinea, *Quat. Res., 4*, 185-205, 1974.

Buck, W.R., Small scale convection induced by passive rifting: The cause of uplift of rift shoulders, *Earth Planet. Sci. Lett., 77*, 362-372, 1986.

Butzer, K.W., Late Pleistocene beaches and wadi alluvia near Marsa Alam, Red Sea Coast, Egypt, *Paleoecol. Afr. Surround. Isl. Antarct. Capetown, 6*, 125-126, 1976.

Chase, C.G., Fluvial landsculpting and the fractal dimension of topography, *Geomorphology, 5*, 39-57, 1992.

Chen, J.H., H. A. Curran, B. White, and G. J. Wasserberg, Precise chronology of the last interglacial period: ^{234}U-^{230}Th data from fossil coral reefs in the Bahamas, *Geol. Soc. Am. Bull., 103*, 82-97, 1991.

Clemens, S., W. Prell, D. Murray, G. Schimmield, and G. Weedon, Forcing mechanisms of the Indian Ocean monsoon, *Nature, 353*, 720-725, 1991.

Friedman, G.M., Identification of carbonate minerals by staining methods, *J. Sediment. Petrol., 29*, 87-97, 1959.

Garfunkel, E., Relation between continental rifting and uplifting: Evidence from Suez rift and northern Red Sea, *Tectonophysics, 150*, 33-49, 1988.

Garrels, R.M., and F.T. Mackenzie, *Evolution of Sedimentary Rocks*, 397 pp., W.W. Norton, New York, 1971.

Greene, D.C., Structural geology of the Quseir area, Red Sea Coast, Egypt, A.M. thesis, 159pp., Univ. of Mass., Amherst, Mass., 1984.

Gvirtzman, G., J. Kronfeld, and B. Buchbinder, Dated coral reefs of southern Sinai (Red Sea) and their implication to Quaternary sea levels, *Mar. Geol., 108*, 29-37, 1992.

Hoang, C.T., and M. Taviani, Stratigraphic and tectonic implications of Uranium-series-dated coral reefs from uplifted Red Sea islands, *Quat. Res., 35*, 264-273, 1991.

Hunt, G.R., Spectral signatures of particulate minerals in the visible and near infrared, *Geophysics, 42*, 501-513, 1977.

Imbrie, J, and J.Z. Imbrie, Modeling the climatic response to orbital variations, *Science, 207*, 943-953, 1980.

Issawi, B., et al., Geology of the Safaga-Quseir coastal plain and of Mohamed Rabah area, *Ann. Geol. Surv. Egypt, 1, 1971.*

Koltermann, C.E., and S.M. Gorelick, Paleoclimatic signature in terrestrial flood deposits, *Science, 256*, 1775-1782, 1992.

Luo, W., Regional geologic mapping of Egyptian Red Sea coast between Quseir and Marsa Alam using Remote Sensing techniques, A.M. thesis, 121 pp., Washington Univ., St. Louis, MO, 1992.

Matthews, R.K., *Dynamic Stratigraphy*, 370 pp., Prentice-Hall, Englewood Cliffs, N.J., 1974.

Matthews, R.K., and C. Frohlich, Forward modeling of Bank-margin carbonate digenesis, *Geology, 15*, 673-676, 1987.

Pieters, C.M., Strength of mineral absorption features in the transmitted component of near-infrared reflected light: First results from RELAB, *J. Geophys. Res., 88*, 1694-1704, 1983.

Rivard, B., R.E. Arvidson, I.J. Duncan, M. Sultan, and B. El Kaliouby, Varnish, sediment, and rock controls on spectral reflectance of outcrops in arid regions, *Geology, 20*, 295-298, 1992.

Sabet, A.H., V.B. Tsogoev, and L.M. Babourin, Geological map, Igla sheet, Eastern Desert, scale 1:100,000, Egypt. Geol. Surv. and Min. Auth., Cairo, Egypt, 1973a.

Sabet, A.H., V.B. Tsogoev, V.V. Bessonenko, and L.M. Babourin, Geological map of the central Eastern Desert (24.5 to 25.5 n), Scale 1:250,000, Egypt. Geol. Surv. and Min. Auth., Cairo, Egypt, 1973b.

Sabet, A.H., V.A. Dyrenko, and Y.M. Polyntsev, Geological map: Umm Gheig Sheet, Eastern Desert, Scale 1:100,000, Egypt. Geol. Surv. and Min. Auth., Cairo, Egypt, 1976.

Said, R., The coastal plain, in *Geology of Egypt*, edited by R. Said, pp. 345-359, A.A. Balkema, Netherlands, Rotterdam, 1990.

Schneiderman, N., and P.A. Sandberg, Calcite-aragonite differentiation by selective staining and scanning electron microscopy, *Quat. Res., 4*, 264-273, 1971.

Steckler, M.S., Uplift and extension at the Gulf of Suez: Indications of induced mantle convection, *Nature, 317*, 135-139, 1985.

Sturchio, N.C., and C.M. Binz, Uranium-series age determination of calcite veins, VC-1 drill core, Valles caldera, New Mexico, *J. Geophys. Res., 93*, 6097-6102, 1988.

Thompson, B.W., *The Climate of Africa*, 300 pp., Oxford University Press, New York, 1965.

Thunell, R.C., S.M. Locke, and D.F. Williams, Glacio-eustatic sea-level control on Red Sea salinity, *Nature, 134*, 601-604, 1988.

Veeh, H., and R. Giegengack, Uranium-series ages of corals from the Red Sea, *Nature, 226*, 155-156, 1970.

R. Arvidson, R. Becker, W. Luo, A. Shanabrook, and M. Sultan, McDonnell Center for the Space Sciences, Department of Earth and Planetary Sciences, Washington University, Campus Box 1169, One Brookings Drive, St. Louis, MO 63130-4899.

Z. El Alfy, Egyptian Geological Survey and Mining Authority, 3 Salah Salem Road, Abbassia, Cairo, Egypt.

Z. Lotfy and A.M. Mahmood, Department of Biological and Geological Sciences, Ain Shams University, Roxy, Cairo, Egypt.

N. Sturchio, Argonne National Laboratory, #205 Office A155, 9700 South Cass Avenue, Argonne, IL 60439

(Received April 2, 1993; revised October 8, 1993;
accepted December 28, 1993.)